Editors' Suggestion

Multistate interferometric measurement of the nonlinear ac Stark shift

Junnosuke Takai,[1] Kosuke Shibata,[1,*] Naota Sekiguchi,[2] and Takuya Hirano[1]
[1]*Department of Physics, Gakushuin University, Tokyo 171-8588, Japan*
[2]*Department of Electrical and Electronic Engineering, Tokyo Institute of Technology, Tokyo 152-8552, Japan*

(Received 24 March 2023; accepted 24 April 2023; published 11 May 2023)

We demonstrate measurement of quadratic ac Stark shifts between Zeeman sublevels in an ^{87}Rb Bose-Einstein condensate using a multistate atomic interferometer. The interferometer can detect a quadratic shift without being affected by relatively large state-independent shifts, thereby improving the measurement precision. We measure quadratic shifts in the total spin $F = 2$ state due to the light being near resonant to the D_1 line. The agreement between the measured and theoretical detuning dependences of the quadratic shifts confirms the validity of the measurement. We also present results on the suppression of nonlinear spin evolution using near-resonant dual-color light pulses with opposite quadratic shifts.

DOI: 10.1103/PhysRevA.107.053308

I. INTRODUCTION

Atom-field interactions often cause shifts in atomic energy levels, referred to as ac Stark shifts in the semiclassical treatment. These shifts often depend on the atomic spin state. Linear and quadratic energy shifts (light shifts) of Zeeman sublevels can arise from spherical tensor operators of rank 1 (vector) and 2 (tensor), respectively, in the irreducible decomposition of the interaction Hamiltonian [1,2]. Quadratic shifts enable advanced quantum state manipulation such as dynamical spin control [3] and nuclear-spin–electronic-spin entanglement [4]. Quadratic shifts have recently been used to generate the Schrödinger kitten state in cold Dy atoms of large spin $J = 8$ [5]. On the other hand, quadratic shifts are often detrimental for precise measurements, such as in atomic clocks. Even a small energy shift can be a dominant uncertainty in state-of-the-art precise measurements. Quadratic shifts are also harmful in spin detection via Faraday rotation [6,7]. In a Faraday rotation measurement, near-resonant light gives a large signal but may also change the atomic spin state through nonlinear spin evolution due to quadratic shifts [2,7,8].

Accurate measurement of quadratic or tensor shifts is important for building a sound basis for quantum control as well as for precise measurements. The tensor shifts in clock transitions in alkali-metal atoms have been measured using the Ramsey method with a hot vapor [9] and a cold-atom fountain [10]. Tensor shifts in cold lanthanide atoms in the ground state have been determined using Kapitza-Dirac diffraction from a pulsed standing wave [11], trap frequency measurement [12,13], and modulation spectroscopy in an optical lattice [14]. In these measurements [9–14], the tensor shift is distinguished from other shifts based on the difference in the frequency dependence of the scalar and tensor shifts and/or the polarization dependence of the tensor shift. Tensor shift measurements distinguished in this way tend to be uncertain due to technical issues, such as imperfect polarization control at the atomic position. It is difficult to precisely determine a tensor shift much smaller than a state-independent scalar shift. This is the case for most atom experiments, although lanthanide atoms can have large tensor polarizability at specific light frequencies [11–14].

In the present study, we demonstrate the detection of quadratic light shifts using a multistate atomic interferometer [15,16] in a Bose-Einstein condensate (BEC) of ^{87}Rb atoms. This scheme is insensitive to state-independent light shifts and directly measures the quadratic light shift, thereby realizing a sensitive measurement by avoiding the uncertainty in distinguishing the tensor shift from other shifts. Direct tensor shift detection is also advantageous in that we can measure the shift in a particular experimental configuration without needing to change light frequencies or polarization. Furthermore, as we can measure the tensor shift without relying on *a priori* theoretical knowledge including the light frequency and polarization dependence of the shift, the measurement may be used to check the validity of a theory. Conversely, by verifying that the measured frequency dependence of the quadratic shift is consistent with the theory, the validity of the measurement scheme is confirmed. We confirm the validity of our measurement in this manner. We also demonstrate suppression of nonlinear spin evolution using dual-color light pulses near the D_1 transition, with the light frequencies and powers chosen on the basis of the light-shift measurement to null the net quadratic shift.

The paper is organized as follows. In Sec. II we present our experimental method and setup. The experimental results are described in Sec. III. We summarize the paper in Sec. IV.

*shibata@qo.phys.gakushuin.ac.jp

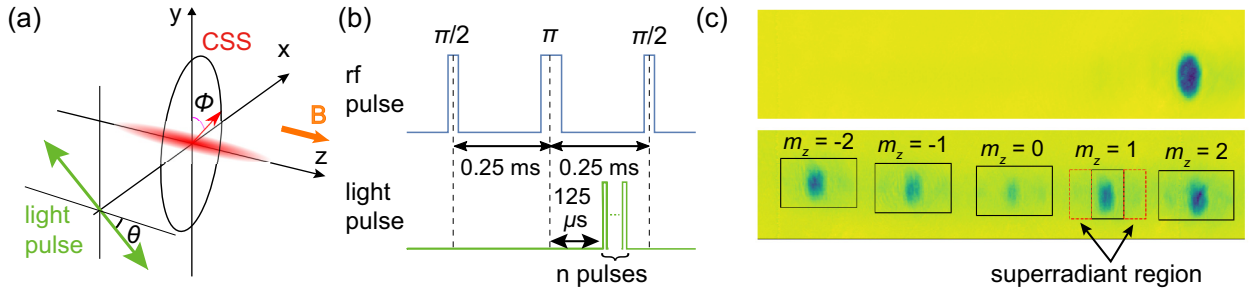

FIG. 1. (a) Experimental configuration. The BEC (shown by a red ellipsoid) in a coherent spin state (CSS), a product of the same single spin states, exhibits Larmor precession after the first rf pulse of the interferometer about the z axis along the bias magnetic field B. A linearly polarized 795-nm light pulse propagates in the x direction through the BEC. The spin evolves from a CSS into another spin state by the light pulse. (b) Time sequence for quadratic shift detection. We use $\pi/2$-π-$\pi/2$ rf pulses to construct an atomic interferometer. A train of n light pulses is applied between the π pulse and last $\pi/2$ pulse. (c) Typical time-of-flight (TOF) images of a BEC measured after the detection sequence. The field of view is 2.1×0.46 mm^2. The top and bottom panels show TOF images without light pulses and with a train of $n = 9$ pulses of $P = 5.71$ mW and $\Delta/2\pi = -840$ MHz, respectively. The black rectangles in the bottom panel indicate the analysis regions for counting the atom number in each magnetic sublevel. The vertical and horizontal axes are along the y and z directions, respectively.

II. EXPERIMENTAL METHOD AND SETUP

The BEC is trapped in a crossed optical trap. The trap is composed of an axial beam at a wavelength of 852 nm and a radial beam at 976 nm. The axial and radial beam waists are approximately 30 and 70 μm, respectively. The axial and radial trap frequencies are measured to be $2\pi \times 16$ and $2\pi \times 123$ Hz, respectively. A bias magnetic field B of 15 μT is applied along the axial beam along the z axis.

The Larmor precession frequency by the bias field is measured to be 105.5 kHz with the use of rf spectroscopy. We initially prepare the atoms in the $|F, m_z\rangle = |2, 2\rangle$ state, where F is the quantum number for the total angular momentum of the atoms in the ground state and m_z denotes the magnetic sublevel.

The experimental configuration for the light-shift measurement is shown in Fig. 1(a). We measure the quadratic light shift due to a light pulse near resonant to the D_1 line ($\lambda = 795$ nm), which propagates in the x direction. The D_1 light is generated by a distributed feedback (DFB) laser and is frequency offset locked to a master external cavity diode laser (ECDL). The frequency of the ECDL is stabilized to the $F = 2 \rightarrow F' = 1$ resonance line, where F' represents the total angular momentum for the excited $^2P_{1/2}$ state. The beam power is controlled by an acousto-optic modulator (AOM). The beam is directed to the atoms through an optical fiber after the AOM. The beam is almost collimated before the atom cell and has a Gaussian profile with a $1/e^2$ radius of $w_0 = 0.75$ mm. We control the polarization state at the atomic position using a half waveplate (HWP) and a quarter waveplate before the atom cell. Just after the cell we adjust the polarization of the light to be linearly polarized. The angle between the polarization plane and the direction of the magnetic field, θ, is adjusted to 54.7°. This angle is chosen for the compatibility with an atomic magnetometer experiment [17], where the nonlinear atom-field interaction is reduced by time averaging [7,17]. The nonlinear interaction, however, does not vanish in this experiment, because the spin direction is almost fixed during light irradiation. The quadratic shift measurement presented below can be performed for any θ.

We perform atomic interferometry with the time sequence depicted in Fig. 1(b). In this sequence, we use the spin echo method to suppress the influence from low-frequency fluctuations of the bias magnetic field. We apply light pulses between the middle π pulse and last $\pi/2$ rf pulse. Each magnetic sublevel experiences an ac Stark shift and acquires a phase shift during the light pulse. Different phase shifts between the magnetic sublevels result in a change in the population of each sublevel after the last $\pi/2$ rf pulse. We measure the sublevel populations by absorption imaging along the x axis after a time of flight of 20.6 ms with Stern-Gerlach spin separation along the z axis [see Fig. 1(a)].

The ac Stark shift due to light near resonant to the D_1 line is derived from the light-shift Hamiltonian [2]

$$\hat{H}_{\text{shift}} = \sum_{F'} \frac{\hbar\Omega_0^2}{4\Delta_{FF'}} \Big[C^{(0)}_{FF'} |\vec{\varepsilon}|^2 + \mathrm{i} C^{(1)}_{FF'} (\vec{\varepsilon}^{\,*} \times \vec{\varepsilon}\,) \cdot \hat{\boldsymbol{F}} + C^{(2)}_{FF'} \big(|\vec{\varepsilon} \cdot \hat{\boldsymbol{F}}|^2 - \tfrac{1}{3} \hat{\boldsymbol{F}}^2 |\vec{\varepsilon}\,|^2 \big) \Big], \tag{1}$$

where $\Delta_{FF'}$ is the amount of light detuning from the transition frequency between the F and F' states, $C^{(k)}_{FF'}$ is a rank-k tensor coefficient representing the angular momentum dependence [2], and $\vec{\varepsilon}$ is the polarization vector for the light. Further, Ω_0 is defined by

$$\Omega_0 = \frac{\langle P_{1/2} || d || S_{1/2} \rangle E}{\hbar}, \tag{2}$$

where $\langle P_{1/2} || d || S_{1/2} \rangle = 2.537 \times 10^{-29}$ C m [18] is the reduced matrix element for the D_1 dipole transition and E is the field amplitude. In addition, Ω_0 can be expressed using the beam power P as

$$\Omega_0 = \frac{\langle P_{1/2} || d || S_{1/2} \rangle}{\hbar} \sqrt{\frac{4P}{\pi c \varepsilon_0 w_0^2}} \equiv \sqrt{\eta P}, \tag{3}$$

where c is the speed of light and ε_0 is the electric constant. Here the beam intensity at the BEC is assumed to be given by $I = 2P/\pi w_0^2$. Hereafter, we consider linearly polarized light, which introduces no vector shift and produces a state-dependent shift solely through the tensor component. The

state-dependent Hamiltonian can be written as

$$\hat{H}_{\rm depend} = \frac{\hbar\Omega_0^2}{4\Delta_{\rm hfs}}\chi(\hat{F}_y\cos\theta + \hat{F}_z\sin\theta)^2, \tag{4}$$

where $\Delta_{\rm hfs} = 2\pi \times 814.5$ MHz is the hyperfine splitting between the $F' = 1$ and $F' = 2$ states and

$$\chi = \sum_{F'} \frac{C^{(2)}_{FF'}\Delta_{\rm hfs}}{\Delta_{FF'}} \tag{5}$$

represents the dependence of the coupling strength on the light frequency. We refer to χ as the coupling coefficient. In an experiment using the ground $F = 2$ state, χ depends on the laser frequency as

$$\chi = \frac{\Delta_{\rm hfs}}{12}\left(\frac{1}{\Delta} - \frac{1}{\Delta - \Delta_{\rm hfs}}\right), \tag{6}$$

where $\Delta \equiv \Delta_{21}$ [see Fig. 3(b)]. Hereafter, we consider detuning with respect to the transition frequency between the $F = 2$ and $F' = 1$ states.

The spin dynamics for $\hat{H}_{\rm depend}$ can be easily described if the quantization axis is selected to be along the direction of the polarization axis, z'. The state before sending the light pulse, $|\psi\rangle = \sum_{m_{z'}} \beta_{m_{z'}}|m_{z'}\rangle$, with $\beta_{m_{z'}}$ the probability amplitude for each sublevel $m_{z'}$ in this frame, evolves under the influence of a rectangular pulse of width τ and power P into

$$|\psi'\rangle = \sum_{m_{z'}} \beta_{m_{z'}} e^{i\chi {m_{z'}}^2 \xi P\tau}|m_{z'}\rangle, \tag{7}$$

where

$$\xi = \frac{\eta}{4\Delta_{\rm hfs}}. \tag{8}$$

Here we consider evolution due to a single pulse for simplicity. The extension to the multipulse case is straightforward. We assume that the pulse width τ is sufficiently shorter than the period of Larmor precession and neglect evolution due to the magnetic field during the pulses. In Eq. (7) we omit the global (state-independent) phase shift, which has no relevance to the population change in the magnetic sublevels. If the spin evolution during the pulse is purely caused by the light shift, the state after the last $\pi/2$ pulse in the m_z basis is written using the Wigner D matrix [16] $D^j(\alpha, \beta, \gamma)$ as

$$|\psi''\rangle = D^2(0, 0, \pi)D^2\left(0, -\frac{\pi}{2}, 0\right) \times D^2(0, -\theta, \phi)^\dagger A D^2(0, -\theta, \phi)|\psi_0\rangle, \tag{9}$$

where $A = {\rm diag}(e^{4i\chi\xi P\tau}, e^{i\chi\xi P\tau}, 1, e^{i\chi\xi P\tau}, e^{4i\chi\xi P\tau})$ represents the time development by light pulses, ϕ is the spin angle in the x-y plane with respect to the y axis at the starting time of the light pulse, and $|\psi_0\rangle = (-1/4, i/2, \sqrt{6}/4, -i/2, -1/4)^T$, where the state is represented in the m_z basis. Here $|\psi_0\rangle$ is a coherent spin state, which is defined as the product state of the individual spin states pointing in the same direction. The spin direction of $|\psi_0\rangle$ is along the y axis. Here $D^j(\alpha, \beta, \gamma)$ is defined in terms of the Euler angles (α, β, γ) around the z, y, and z axes, respectively, as

$$D^j_{q'q}(\alpha, \beta, \gamma) = \langle jq'|\hat{R}(\alpha, \beta, \gamma)|jq\rangle, \tag{10}$$

where $\hat{R}(\alpha, \beta, \gamma) = e^{-i\alpha\hat{j}_z}e^{-i\beta\hat{j}_y}e^{-i\gamma\hat{j}_z}$ is the rotational operator [19]. We calculate the magnetization $m = \langle\psi''|\hat{F}_z|\psi''\rangle$ using Eq. (9). The calculated m is a function of $\chi\xi P\tau$. Details of the calculation of m are presented in the Appendix. We note that $m = 2\cos^3(\chi\xi P\tau)$ if $\theta = 0$ [20].

III. RESULTS

A. Measurement of quadratic light shifts

We first detect quadratic light shifts produced by a single pulse of $\Delta/2\pi = -840$ MHz, which induces fewer light-assisted collisional atom losses [17]. The pulse has an almost rectangular shape and its length is fixed to $\tau = 667$ ns. The pulse length is much shorter than the inverse of the Larmor frequency and the spin evolution by the magnetic field during the pulse is negligible, as assumed in the calculation above. The pulse is applied 0.125 ms after the π pulse, when the spin orientation is along the x axis ($\phi = \pi/2$). This interval ensures negligible overlap between the light and rf pulses. The rf π pulse has a Gaussian envelope of 28.78 μs width and the spin evolution due to light is not practically affected by the rf field. We confirm the spin direction by spin-sensitive phase contrast imaging [17].

We observe changes in the sublevel population using a Stern-Gerlach measurement, as shown in Fig. 1(c). We experimentally obtain the magnetization using

$$m = \frac{\sum_i iN_i}{N_{\rm tot}}, \tag{11}$$

where N_i is the number of atoms in the $|F, m_z = i\rangle$ state ($i = -2, -1, 0, 1, 2$) after the read-out pulse and $N_{\rm tot} = \sum_i N_i$ is the total number of atoms. The magnetization is plotted as a function of the beam intensity normalized by the effective far-detuned saturation intensity $I_{\rm sat} = 4.4876(43)$ mW/cm^2 [21]. We fit the data using $(1 - \delta p)\langle\psi''|\hat{F}_z|\psi''\rangle$, where δp is introduced to account for experimental imperfect state preparation and control. Imperfect state control results from magnetic-field noise. The effect of the ac noise is not perfectly removed by the spin echo and the slow magnetic-field drift makes the rf off-resonance. The fluctuation of the spin direction after the interferometric sequence due to the imperfect spin control results in decreased mean magnetization around $m = 2$. Fluctuation in the initial spin direction also results from magnetic-field noise orthogonal to the bias field. State preparation in the experiment can be imperfect due to, for example, spin flip during atom transfer from the magnetic trap for precooling atoms into the optical trap. In the fitting [red solid line in Fig. 2(a)], we use Eq. (9) with $\theta = 54.7^\circ$ and $\phi = 90^\circ$, in correspondence with the experiment. The fitting gives $\chi = -0.0404(8)$. The value in parentheses denotes the standard deviation of χ calculated from three sets of data. In this fitting δp is 0.0132(7), where the value in parentheses represents the standard error of the fit.

Next we measure the quadratic light shifts for other light frequencies with positive detunings $\Delta/2\pi = \{240, 340, 440, 540, 640\}$ MHz. The results for each detuning are depicted in Figs. 2(b)–2(f). We observe large changes in m. For these positive detunings, χ is much larger than that for $\Delta/2\pi = -840$ MHz and the observed large change in m is reasonable.

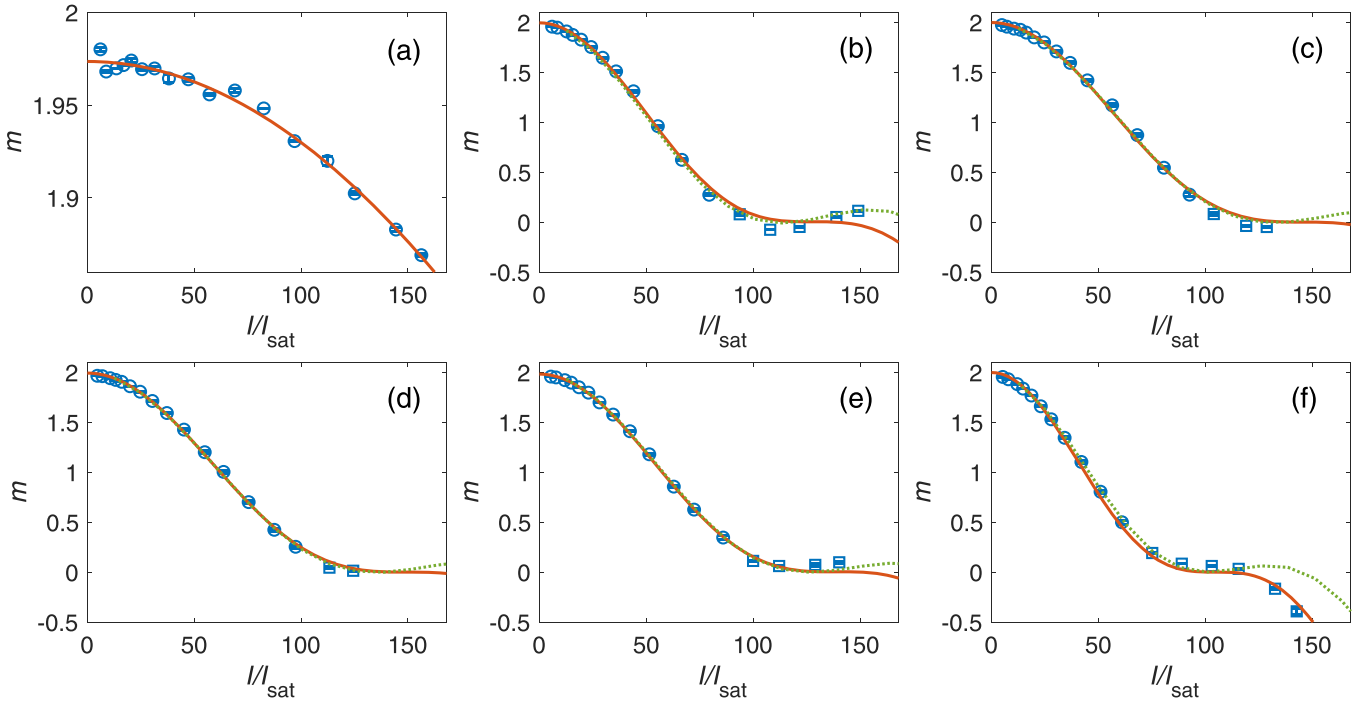

FIG. 2. Magnetization m for $\Delta/2\pi$ of (a) -840, (b) 240, (c) 340, (d) 440, (e) 540, and (f) 640 MHz as a function of $I/I_{\rm sat}$. The blue symbols (circles and squares) represent the measured magnetization. The circle data points are used for fitting (see the text for details) and the red solid lines are the fitting curves. The green dotted line is the simulated magnetization including the spontaneous-emission effect. The calculation and simulation are performed for a single pulse of $\tau = 667$ ns.

The spontaneous-emission rates also become large for these detunings and optical pumping due to spontaneous emission may also result in spin change. To evaluate the contribution of spontaneous emissions, we numerically calculate the dynamics of the magnetization using an atomic master equation including spontaneous emission [22]. A theoretically predicted value of the coupling coefficient $\chi_{\rm theor}$ is used in the simulation. We plot the simulation results in Fig. 2 (green dotted lines). The numerical simulation indicates that the spontaneous emissions are not negligible for beam powers higher than approximately 5 mW ($I/I_{\rm sat} = 126$), which we were not able to investigate in detail due to the limited available beam power. In the fitting shown by red solid lines in Figs. 2(b)–2(f), to obtain experimental values of the coupling coefficient $\chi_{\rm expt}$, we use data points at beam powers for which the magnetization obtained by the simulation differs from the matrix calculation by less than 0.06 to lessen the effect of spontaneous emissions on the estimation of χ. The fitted values of $\chi_{\rm expt}$ are shown in Table I.

The frequency dependence of $\chi_{\rm expt}$ is consistent with the theoretical curve given by Eq. (6), as shown in Fig. 3(a). Note that interferometric detection does not reveal the sign of χ. We determine the sign of χ at each Δ in Fig. 3(a) to coincide with the theoretically determined sign. We also note that the exact determination of χ requires precise calibration of the beam intensity at the atom position. It is more appropriate to analyze the ratio between $\chi_{\rm expt}$ and $\chi_{\rm theor}$ to estimate the validity of the measurement. This ratio is shown in Table I. The sample standard deviation of the ratios, which represents the precision of the measurement, is 0.02 (2%).

B. Suppression of nonlinear spin evolution

We also demonstrate suppression of spin evolution due to a quadratic shift by using near-resonant dual-color light pulses. From Eq. (6) we can see that χ is positive if $0 < \Delta < \Delta_{\rm hfs}$ and negative otherwise. If we combine negative ($\Delta < 0$) and positive ($0 < \Delta < \Delta_{\rm hfs}$) detuned light with a power ratio of $p_{\rm neg}/p_{\rm pos} = \chi_{\rm pos}/\chi_{\rm neg}$, the quadratic light shift should vanish and nonlinear spin evolution should be suppressed. We use the DFB laser used in the above experiment at a fixed detuning of $\Delta_-/2\pi = -840$ MHz. We prepare another ECDL for quadratic shift compensation. The ECDL is frequency offset locked to the master ECDL and its detuning is set to $\Delta_+/2\pi = \{240, 340, 440, 540, 640\}$ MHz. The two laser beams are mixed at a nonpolarizing beam splitter (NPBS) before the AOM for power control. We adjust the ratio of the DFB laser power to the ECDL power using a HWP and PBS

TABLE I. Measured and theoretical coupling coefficients and power ratios for quadratic shift cancellation.

$\frac{\Delta}{2\pi}$ (MHz)	$\chi_{\rm expt}$	$\chi_{\rm expt}/\chi_{\rm theor}$	$r_{\rm expt}$	$r_{\rm theor}$	$r_{\rm expt}/r_{\rm theor}$
-840	-0.0404	1.016			
240	0.411	1.025	10.17	10.08	1.01
340	0.356	1.039	8.81	8.61	1.02
440	0.351	1.045	8.68	8.43	1.03
540	0.379	1.017	9.39	9.37	1.00
640	0.486	0.982	12.02	12.44	0.97

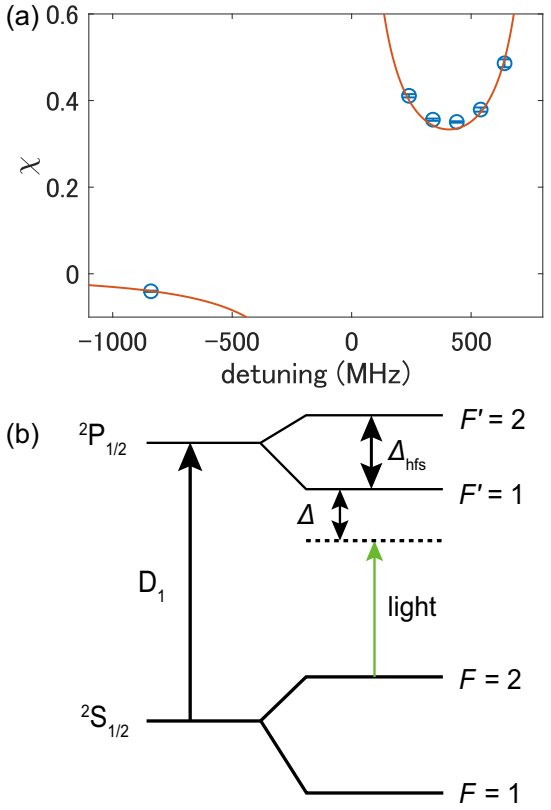

FIG. 3. (a) Dependence of the coupling coefficient χ on detuning. The blue circles represent the coefficients obtained from the experiments. The error bar for each circle represents the standard deviation over three experimental runs. The red solid line is the theoretical curve given by Eq. (6). (b) Energy diagram for ^{87}Rb relevant to the experiment.

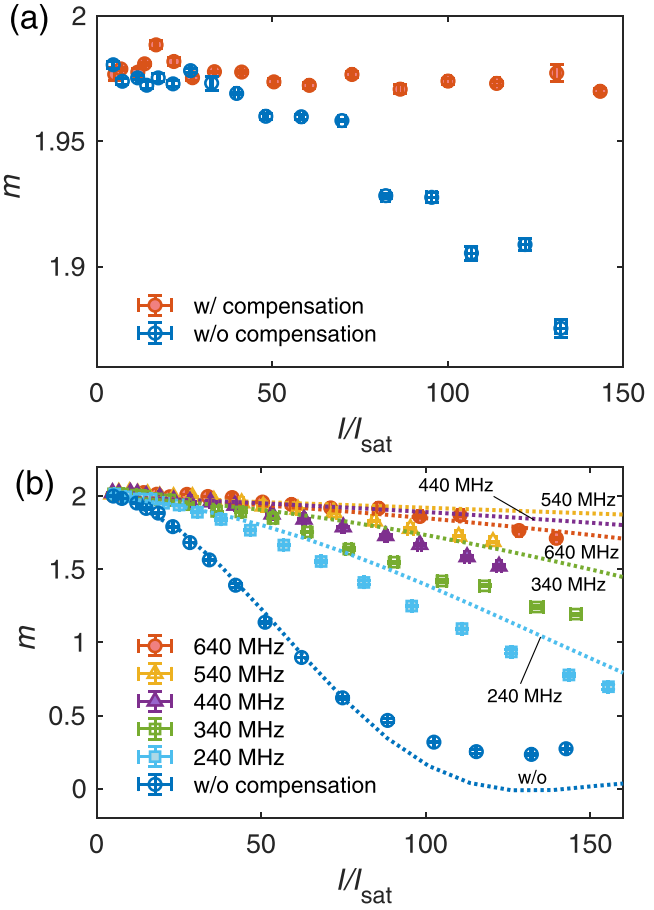

FIG. 4. Magnetization with and without compensation as a function of intensity in saturation units. (a) Magnetization for a single pulse. The open blue circles represent the magnetization without compensation (with only the negative-detuned light). The data represented by closed red circles are taken with the compensation light with $\Delta_+/2\pi = 640$ MHz added. (b) Magnetization for $n = 9$ pulses. The magnetization values with compensation light of $\Delta_+/2\pi = 640$, 540, 440, 340, and 240 MHz are plotted by closed red circles, open yellow triangles, closed purple triangles, open green squares, and closed cyan squares, respectively. The open blue circles represent the magnetization without compensation. The magnetization by the numerical simulation including spontaneous emissions is represented by the dotted line with text describing the pulse condition.

before the NPBS. The ratios used in the experiment r_{expt} are listed in Table I. The values of r_{expt} are close to the theoretical optimal ratios

$$r_{\text{theor}} = \left(\frac{1}{\Delta_+} - \frac{1}{\Delta_+ - \Delta_{\text{hfs}}}\right) \Big/ \left(\frac{1}{\Delta_-} - \frac{1}{\Delta_- - \Delta_{\text{hfs}}}\right). \tag{12}$$

We observe that the change in magnetization for the pulse mixture is much less than that for the single negative-detuned pulse. We show the results for $\Delta_+/2\pi = 640$ MHz light compensation and without compensation in Fig. 4(a). We apply $n = 9$ pulses to observe the changes in magnetization more clearly. We set the interval between pulses to 9.5 μs, equal to the period of Larmor precession, in order to apply all pulses when the spin is directed to the probe propagation direction. The results with compensation light pulses with $\Delta_+/2\pi =$ 240, 340, 440, 540, 640 MHz are plotted in Fig. 4(b).

The magnetization changes with increasing power even with compensation. This change is considered to be due to spin relaxation by optical pumping. We also observe that the size of the change depends on the detuning of the compensation beam Δ_+. The closer the frequency to the $F = 2 \to F' = 1$ resonance, the greater the magnetization change. The frequency dependence can be understood as follows. The polarization component of $\hat{e}_y - i\hat{e}_z$ induces the $\Delta m_x = -1$ transition, as shown in Fig. 5. The coupling strength to the $F' = 1$ state is three times stronger than that to the $F' = 2$ state. The increase in the magnetization change as Δ approaches 0 is related to this difference in coupling strength. The frequency dependence of the magnetization change is confirmed by a numerical simulation. The simulated change is minimum at $\Delta_+/2\pi = 540$ MHz. This is consistent with the simple estimation of the relaxation rate given by the product of the scattering rate (approximately proportional to $3/\Delta_{21}^2 + 1/\Delta_{22}^2$) and the beam power required for the quadratic shift compensation (proportional to $1/\Delta_{21} - 1/\Delta_{22}$). The magnetization change in the experiment is larger than that in the simulation including the spontaneous emissions, especially for detuning from 340 to 540 MHz.

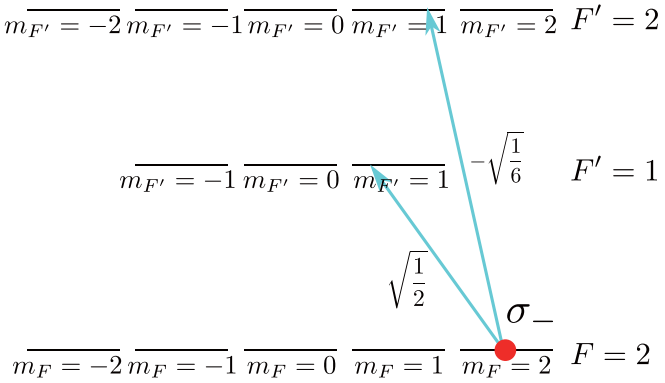

FIG. 5. Coupling strength between the $|F, m_F\rangle = |2, 2\rangle$ state and excited states. The x axis is taken as the quantization axis here. The blue arrows represent the allowed transitions. The number next to each arrow is the dipole matrix element, expressed as multiples of $\langle P_{1/2}||d||S_{1/2}\rangle$.

A possible cause of the faster magnetization change in the experiment than the simulation is the superradiance [23–25]. Optical pumping can be enhanced if the Raman superradiance among the magnetic sublevels occurs. In fact, we observe atoms kicked by superradiant scattering when the beam is strong. We show time-of-flight images and one-dimensional atom density profiles with strong $n = 9$ pulses in Fig. 6. We observe atom density peaks at both sides of the normal component along the z axis, which is ascribed to atoms kicked by the superradiance. The kick direction is consistent with the expected endfire mode. We evaluate the proportion of the number of kicked atoms $N_{\rm side}$ to the nonkicked BEC component $N_{\rm c}$. The population in a state other than the $m_z = 2$ state should reflect the optical pumping and the ratio of the superradiant component can be a measure of optical pumping

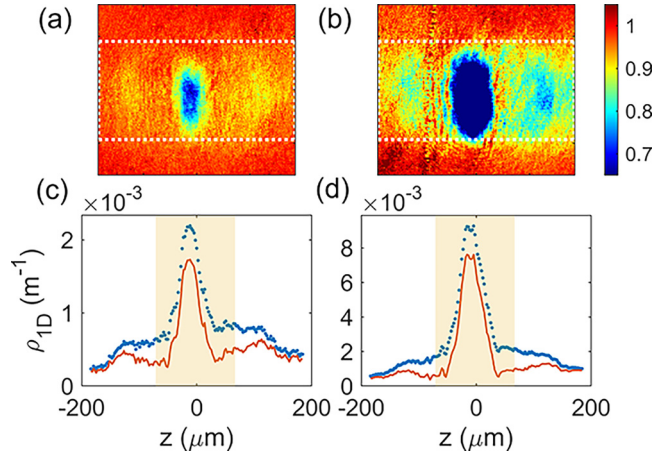

FIG. 6. Superradiance after applying nine dual-color pulses with $\Delta_-/2\pi = -840$ MHz and $\Delta_+/2\pi = -640$ MHz. Here $I/I_{\rm sat}$ is 140. The color represents optical transmission. Absorption by the estimated thermal component is subtracted in these images. The field of view is 0.32 mm (vertical, y) × 0.37 mm (horizontal, z). (c) and (d) The 1D profile obtained by vertically integrating the data in the white dotted box in (a) and (b), respectively. The blue points and red solid line represent the densities without and with thermal component subtraction. The number of atoms in the shaded area is counted as $N_{\rm c}$.

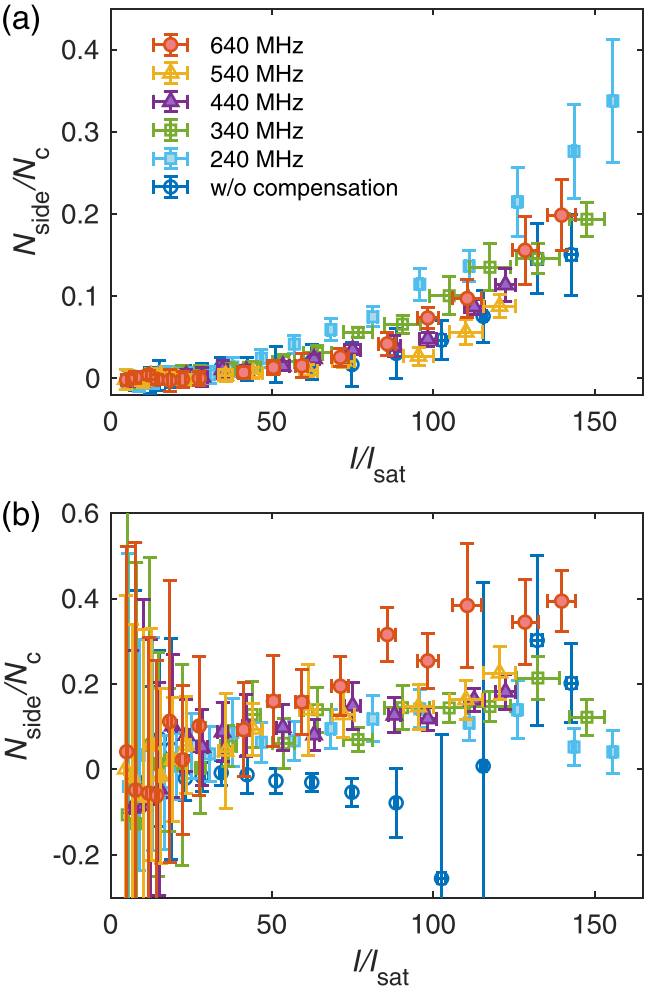

FIG. 7. Evaluation of the superradiance. Proportion of atoms kicked by superradiance for (a) $m_z = 2$ and (b) $m_z = 1$ as a function of beam intensity in saturation units. The ratio $N_{\rm side}/N_{\rm c}$, with compensation light of $\Delta_+/2\pi = 640$, 540, 440, 340, and 240 MHz, is plotted by closed red circles, open yellow triangles, closed purple triangles, open green squares, and closed cyan squares, respectively. Positive-detuned light for compensation is not applied for data represented by open blue circles. The intensity along the horizontal axis does not include that of the compensation beam.

enhancement by superradiance, provided the spin evolution due to the nonlinear light shift is sufficiently small. In the analysis, we count the number of atoms in the regions adjacent to the zero-moment component as $N_{\rm side}$ and that in the center region, represented by the shaded area in Figs. 6(c) and 6(d), as $N_{\rm c}$. The thermal component is subtracted before the counting. We obtain the thermal component distribution by fitting a Gaussian function to the wings of the vertical density profile of the $m_z = 2$ state. The thermal component in the $m_z = 1$ state is estimated from the ratio between the number of atoms in the $m_z = 1$ and 2 states, because the estimation by fitting to the $m_z = 1$ profile is uncertain when there are few atoms in the $m_z = 1$ state. Atom number offset remaining in the case of weak light is also excluded from the counting.

We plot $N_{\rm side}/N_{\rm c}$ for the magnetic sublevels of $m_z = 1$ and 2 in Fig. 7. The data in Fig. 7 are taken with $n = 9$ pulses. We

observe a qualitative difference in the $m_z = 1$ case between with and without the compensation beam [Fig. 7(b)]. While the ratio grows at around $I/I_{\rm sat} = 130$ without the compensation beam (only with the red-detuned beam), the ratio starts to grow at a lower power when the compensation beam is added. This difference should be related to the higher photon scattering rate for the case with the compensation beam. The compensation beam has a larger scattering rate per intensity due to smaller detuning and contribution from the $F' = 2$ state. Such a difference is not observed for the $m_z = 2$ case [Fig. 7(a)]. A lower threshold intensity is expected due to the coupling strength being twice higher than that for the $m_z = 1$ case. The superradiant component ratio in the $m_z = 1$ state may reflect the enhancement of magnetization change by superradiance, as mentioned above. The result implies enhancement of at most several tens of percent. The observed excessive magnetization change, however, is not fully explained by the enhanced optical pumping. The detuning dependence of the excessive change differs from that of the superradiant component ratio. An advanced multilevel simulation is necessary for quantitative evaluation of the superradiant effect on the magnetic sublevel change.

The Raman superradiance [26] to the $F = 1$ state should also contribute to the scattering rate enhancement. State-selective imaging using repumping light will enable the evaluation of such hyperfine Raman superradiance, although we measure atoms in the $F = 2$ state only in this work. We also measure the atom number loss, which changes the population among the magnetic sublevels and causes spin relaxation. We note that the observed loss includes the hyperfine pumping effect, because we measure the atoms in the $F = 2$ state. However, we do not observe a significant dependence of the loss rates on Δ_+, while the observed excessive magnetization change depends on Δ_+.

The larger than expected magnetization change might be partly due to the enhancement of spontaneous emission near the critical temperature for Bose-Einstein condensation [27]. We initially prepare atoms at a temperature T of $0.6T_{\rm c}$, where $T_{\rm c}$ is the critical temperature. The $T/T_{\rm c}$ in our experiment is comparable to that in [27], which reported the enhancement factor of 3. The effect of this enhancement on the magnetization change might be minor, however, because it would not significantly increase the Raman scattering [28].

IV. CONCLUSION AND OUTLOOK

We have demonstrated the successful measurement of quadratic light shifts using an atom interferometer. The measured dependence of the shift due to detuning is consistent with the theoretical prediction. In addition, we suppressed the influence of nonlinear light shifts by using dual-color light pulses. Dual-color light is applicable to high-precision measurement in a probe, especially for BEC magnetometers [17]. A dual-color probe is useful not only for improving the signal-to-noise ratio in spin measurements by increasing the probe strength, but also for preventing disturbances when creating a spin squeezed state via quantum nondemolition measurements [29–33].

The multistate interferometric measurement demonstrated here can be applied not only to a Bose condensed gas but also to more general situations. The method works if the atom number in each magnetic sublevel can be individually measured; it is possible to perform a similar measurement for a cold thermal gas. An interesting extension is to measure the tensor polarizability of excited states. If one can induce a sufficient phase shift and perform a spin measurement within the lifetime of the excited state, the tensor polarizability of the excited state can be measured. The polarizability of excited states may give rich information on the coupling strengths of atoms. The precise measurement of the polarizability of the excited state should be important for ultraprecise measurement such as atomic clocks.

The current main limiting source of the measurement precision is imperfect spin control and state preparation. These noises increase the uncertainty in the measured magnetization, thereby degrading the sensitivity of the quadratic shift measurement. The relative fluctuation of the measured magnetization m in the experiment is 0.01 in the range of $m = 0$–1.5. The current sensitivity will be improved by reducing the magnetic-field fluctuation. The magnetic field slowly drifts by several tens of nT in our environment, which makes the rf pulse slightly off-resonant and can induce the spin direction error of 10^{-2}. The field stabilization within nT order is possible using the appropriate technique [34]. The optimization of the echo interval may reduce noise due to the ac field. The improvement of the initial spin state preparation by spin cleaning using a microwave transition [35] may also lead to better precision.

Further improvements of this measurement scheme are feasible. Reducing technical noises in absorption imaging will lead to higher sensitivity. The bias magnetic field may produce a slight difference between the experimental data and the theoretical prediction calculated by the Wigner D matrix and interaction Hamiltonian, in which we have neglected the spin evolution due to the magnetic field. Therefore, to improve the estimation accuracy for the coupling coefficients, it may be effective to use a low magnetic field. These improvements may make it possible to estimate physical quantities such as transition matrix elements and hyperfine splittings.

ACKNOWLEDGMENTS

This work was supported by the MEXT Quantum Leap Flagship Program (MEXT Q-LEAP) Grant No. JPMXS0118070326, JSPS KAKENHI Grant No. JP19K14635, and the Asahi Glass Foundation.

APPENDIX: CALCULATION OF THE MAGNETIZATION

We explain how to obtain the calculated magnetization used for the fitting to the data shown in Fig. 2. The main part of the calculation is to calculate the product of five matrices (four Wigner D matrices and A) on the right-hand side of Eq. (9). Because we treat the $F = 2$ state in the experiment, each matrix has $5^2 = 25$ elements.

Here we provide an explicit expression of the Wigner D matrix. The Wigner D matrix can be written as

$$D^{j}_{q'q}(\alpha,\beta,\gamma) = \langle jq'|\hat{R}(\alpha,\beta,\gamma)|jq\rangle = e^{-im'\alpha} d^{j}_{m'm}(\beta) e^{-im'\gamma}, \tag{A1}$$

where

$$d^{j}_{m'm}(\beta) = \langle jm'|e^{-i\beta\hat{j}_y}|jm\rangle. \tag{A2}$$

The $d^{2}_{m'm}(\beta)$ are given by

$$d^{2}_{22}(\beta) = \tfrac{1}{4}(1+\cos\beta)^2,$$
$$d^{2}_{21}(\beta) = -\tfrac{1}{2}\sin\beta(1+\cos\beta),$$
$$d^{2}_{20}(\beta) = \sqrt{\tfrac{3}{8}}\sin^2\beta,$$
$$d^{2}_{2-1}(\beta) = -\tfrac{1}{2}\sin\beta(1-\cos\beta),$$
$$d^{2}_{2-2}(\beta) = \tfrac{1}{4}(1-\cos\beta)^2,$$
$$d^{2}_{11}(\beta) = \tfrac{1}{2}(2\cos^2\beta+\cos\beta-1),$$
$$d^{2}_{10}(\beta) = \sqrt{\tfrac{3}{8}}\sin 2\beta,$$
$$d^{2}_{1-1}(\beta) = \tfrac{1}{2}(-2\cos^2\beta+\cos\beta+1),$$
$$d^{2}_{00}(\beta) = \tfrac{1}{2}(3\cos^2\beta-1),$$
$$d^{2}_{m'm}(\beta) = d^{2}_{-m'-m}(\beta).$$

Because $A = \mathrm{diag}(e^{4i\chi\xi P\tau}, e^{i\chi\xi P\tau}, 1, e^{o\chi\xi P\tau}, e^{4i\chi\xi P\tau})$, each element of the product of the five matrices is in general a function of $\chi\xi P\tau$. Therefore, $m = \langle\psi''|\hat{F}_z|\psi''\rangle$ is a function of $\chi\xi P\tau$, as mentioned in the main text. We perform symbolic calculation of m and the fitting by *Mathematica*, instead of writing out explicit expression of the calculated magnetization.

[1] J. M. Geremia, J. K. Stockton, and H. Mabuchi, Tensor polarizability and dispersive quantum measurement of multilevel atoms, Phys. Rev. A **73**, 042112 (2006).

[2] I. H. Deutsch and P. S. Jessen, Quantum control and measurement of atomic spins in polarization spectroscopy, Opt. Commun. **283**, 681 (2010).

[3] S. Chaudhury, S. Merkel, T. Herr, A. Silberfarb, I. H. Deutsch, and P. S. Jessen, Quantum Control of the Hyperfine Spin of a Cs Atom Ensemble, Phys. Rev. Lett. **99**, 163002 (2007).

[4] T. Fernholz, H. Krauter, K. Jensen, J. F. Sherson, A. S. Sørensen, and E. S. Polzik, Spin Squeezing of Atomic Ensembles via Nuclear-Electronic Spin Entanglement, Phys. Rev. Lett. **101**, 073601 (2008).

[5] T. Chalopin, C. Bouazza, A. Evrard, V. Makhalov, D. Dreon, J. Dalibard, L. A. Sidorenkov, and S. Nascimbene, Quantum-enhanced sensing using non-classical spin states of a highly magnetic atom, Nat. Commun. **9**, 4955 (2018).

[6] T. Isayama, Y. Takahashi, N. Tanaka, K. Toyoda, K. Ishikawa, and T. Yabuzaki, Observation of Larmor spin precession of laser-cooled Rb atoms via paramagnetic Faraday rotation, Phys. Rev. A **59**, 4836 (1999).

[7] G. A. Smith, S. Chaudhury, A. Silberfarb, I. H. Deutsch, and P. S. Jessen, Continuous Weak Measurement and Nonlinear Dynamics in a Cold Spin Ensemble, Phys. Rev. Lett. **93**, 163602 (2004).

[8] G. Colangelo, R. J. Sewell, N. Behbood, F. M. Ciurana, G. Triginer, and M. W. Mitchell, Quantum atom-light interfaces in the Gaussian description for spin-1 systems, New J. Phys. **15**, 103007 (2013).

[9] F. Levi, J. Camparo, B. Francois, C. E. Calosso, S. Micalizio, and A. Godone, Precision test of the ac Stark shift in a rubidium atomic vapor, Phys. Rev. A **93**, 023433 (2016).

[10] G. A. Costanzo, S. Micalizio, A. Godone, J. C. Camparo, and F. Levi, ac Stark shift measurements of the clock transition in cold Cs atoms: Scalar and tensor light shifts of the D_2 transition, Phys. Rev. A **93**, 063404 (2016).

[11] W. Kao, Y. Tang, N. Q. Burdick, and B. L. Lev, Anisotropic dependence of tune-out wavelength near Dy 741-nm transition, Opt. Express **25**, 3411 (2017).

[12] J. H. Becher, S. Baier, K. Aikawa, M. Lepers, J.-F. Wyart, O. Dulieu, and F. Ferlaino, Anisotropic polarizability of erbium atoms, Phys. Rev. A **97**, 012509 (2018).

[13] C. Ravensbergen, V. Corre, E. Soave, M. Kreyer, S. Tzanova, E. Kirilov, and R. Grimm, Accurate Determination of the Dynamical Polarizability of Dysprosium, Phys. Rev. Lett. **120**, 223001 (2018).

[14] M. Kreyer, J. H. Han, C. Ravensbergen, V. Corre, E. Soave, E. Kirilov, and R. Grimm, Measurement of the dynamic polarizability of Dy atoms near the 626-nm intercombination line, Phys. Rev. A **104**, 033106 (2021).

[15] J. Petrovic, I. Herrera, P. Lombardi, F. Schäfer, and F. S. Cataliotti, A multi-state interferometer on an atom chip, New J. Phys. **15**, 043002 (2013).

[16] M. Sadgrove, Y. Eto, S. Sekine, H. Suzuki, and T. Hirano, Ramsey interferometry using the Zeeman sublevels in a spin-2 Bose gas, J. Phys. Soc. Jpn. **82**, 094002 (2013).

[17] N. Sekiguchi, K. Shibata, A. Torii, H. Toda, R. Kuramoto, D. Fukuda, and T. Hirano, Sensitive spatially resolved magnetometry using a Bose-condensed gas with a bright probe, Phys. Rev. A **104**, L041306 (2021).

[18] R. Loudon, *The Quantum Theory of Light* (Oxford University Press, Oxford, 2000).

[19] J. J. Sakurai and J. Napolitano, *Modern Quantum Mechanics*, 2nd ed. (Cambridge University Press, Cambridge, 2017).

[20] M. Kitagawa and M. Ueda, Squeezed spin states, Phys. Rev. A **47**, 5138 (1993).

[21] D. A. Steck, Rubidium 87 D line data, revision 2.2.2. (2021), available at http://steck.us/alkalidata.

[22] W. Happer, Y.-Y. Jau, and T. Walker, *Optically Pumped Atoms* (Wiley, New York, 2010).

[23] R. H. Dicke, Coherence in spontaneous radiation processes, Phys. Rev. **93**, 99 (1954).

[24] M. Gross and S. Haroche, Superradiance: An essay on the theory of collective spontaneous emission, Phys. Rep. **93**, 301 (1982).

[25] N. E. Rehler and J. H. Eberly, Superradiance, Phys. Rev. A **3**, 1735 (1971).

[26] D. Schneble, G. K. Campbell, E. W. Streed, M. Boyd, D. E. Pritchard, and W. Ketterle, Raman amplification of matter waves, Phys. Rev. A **69**, 041601(R) (2004).

[27] P. C. Bons, R. de Haas, D. de Jong, A. Groot, and P. van der Straten, Quantum Enhancement of the Index of Refraction in a Bose-Einstein Condensate, Phys. Rev. Lett. **116**, 173602 (2016).

[28] Y.-K. Lu, Y. Margalit, and W. Ketterle, Bosonic stimulation of atom-light scattering in an ultracold gas, Nat. Phys. **19**, 210 (2023).

[29] A. Kuzmich, N. Bigelow, and L. Mandel, Atomic quantum nondemolition measurements and squeezing, Europhys. Lett. **42**, 481 (1998).

[30] L. K. Thomsen, S. Mancini, and H. M. Wiseman, Spin squeezing via quantum feedback, Phys. Rev. A **65**, 061801(R) (2002).

[31] L. Thomsen, S. Mancini, and H. Wiseman, Continuous quantum nondemolition feedback and unconditional atomic spin squeezing, J. Phys. B **35**, 4937 (2002).

[32] A. Silberfarb and I. H. Deutsch, Continuous measurement with traveling-wave probes, Phys. Rev. A **68**, 013817 (2003).

[33] D. Hemmer, E. Montaño, B. Q. Baragiola, L. M. Norris, E. Shojaee, I. H. Deutsch, and P. S. Jessen, Squeezing the angular momentum of an ensemble of complex multilevel atoms, Phys. Rev. A **104**, 023710 (2021).

[34] Z.-X. Duan, W.-T. Wu, Y.-T. Lin, and S.-J. Yang, Simple and active magnetic-field stabilization for cold atom experiments, Rev. Sci. Instrum. **93**, 123201 (2022).

[35] Y. Eto, H. Shibayama, K. Shibata, A. Torii, K. Nabeta, H. Saito, and T. Hirano, Dissipation-Assisted Coherence Formation in a Spinor Quantum Gas, Phys. Rev. Lett. **122**, 245301 (2019).